# An efficient integrated two-color source for heralded single photons

## S Krapick[1], H Herrmann, V Quiring, B Brecht, H Suche and Ch Silberhorn

Integrated Quantum Optics Group, Department of Physics, University of Paderborn, Warburger Straße 100, D-33098 Paderborn, Germany
E-mail: krapick@mail.upb.de

**Abstract.** We present a pulsed and integrated, highly non-degenerate parametric down-conversion (PDC) source of heralded single photons at telecom wavelengths, paired with heralding photons around 800 nm. The active PDC section is combined with a passive, integrated wavelength division demultiplexer on-chip, which allows for the spatial separation of signal and idler photons with efficiencies of more than 96.5%, as well as with multi-band reflection and anti-reflection coatings which facilitate low incoupling losses and a pump suppression at the output of the device of more than 99%. Our device is capable of preparing single photons with efficiencies of 60% with a coincidences-to-accidentals ratio exceeding 7400. Likewise, it shows practically no significant background noise compared to continuous wave realizations. For low pump powers, we measure a conditioned second-order correlation function of $g^{(2)} = 3.8 \times 10^{-3}$, which proves almost pure single-photon generation. In addition, our source can feature a high brightness of $\langle n_{\text{pulse}} \rangle = 0.24$ generated photon pairs per pump pulse at pump power levels below $100\,\mu\text{W}$. The high quality of the pulsed PDC process in conjunction with the integration of highly efficient passive elements makes our device a promising candidate for future quantum networking applications, where an efficient miniaturization plays a crucial role.

[1] Author to whom any correspondence should be addressed.

**IOP** Institute of Physics · DEUTSCHE PHYSIKALISCHE GESELLSCHAFT

## Contents

## 1. Introduction

Recent progress in the field of quantum information processing has highlighted the prospects of using integrated optic devices for quantum applications [1–5]. Integrated quantum photonics offers several advantages in comparison with free-space experimental setups with bulk optic components [6]. The miniaturization of systems with increased complexity not only drastically reduces the required space and paves the way for future commercialization, but also enables the implementation of optical networks with a large number of optical modes and an extremely high stability.

In 2008 Politi *et al* [7] demonstrated the first quantum interference and photonic gates on-chip, whereas different groups developed sophisticated and integrated experiments with two-photon interference [8, 9] or photon entanglement [10, 11], controlled qubit operations [12] and the controlled phase shifts in linear optical circuits [5, 13]. In 2012, Metcalf *et al* [14] realized the first three-photon experiment inside a linear optical network, and recent research on boson sampling in an integrated device demonstrates four-photon quantum interference [15].

However, in all these experiments the preparation of the photon pairs has actually been performed outside the integrated devices employing traditional bulk crystal parametric down-conversion (PDC) sources. The efficient coupling between these sources and the integrated circuit remains a bottleneck for designing systems with increasing complexity.

On the other hand, remarkable efforts have been devoted to the development of integrated PDC sources for photon pair generation inside channel waveguides [16–23] over the last few decades. The main benefits of guided-wave PDC processes include high conversion efficiencies and spatial mode control.

Among several fabrication techniques with different nonlinear materials used for the implementation of PDC sources (see e.g. [17, 24–27]), titanium-indiffusion is a standard method
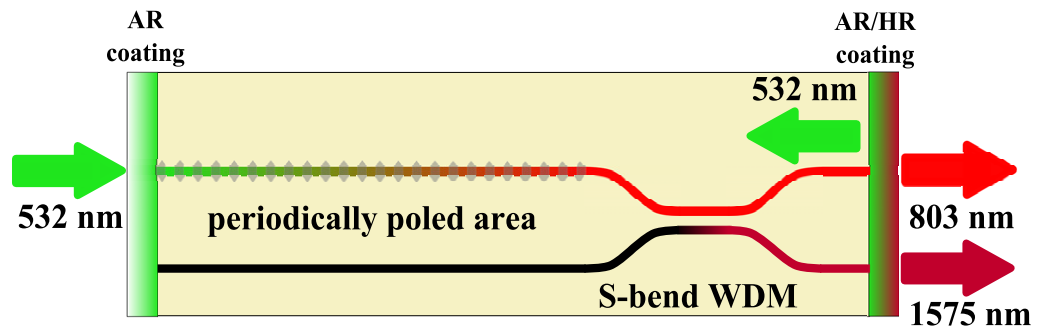
**Figure 1.** Schematic representation of the Ti : PPLN photon pair source.

to manufacture waveguides in lithium niobate (Ti:LN). It provides extremely low loss [28] and the guiding of both polarizations.

In this paper, we report on the fabrication and analysis of an integrated type-I PDC source in titanium-indiffused periodically poled Z-cut lithium niobate waveguides (Ti:PPLN) for heralded single photons. We combine an optically active component providing PDC of high brightness with a passive element on-chip allowing for excellent spatial separation of the converted, highly non-degenerate photon pairs. This enables us, on the one hand, to transmit prepared PDC states via low-loss fibers at the telecom L-band around 1575 nm and, on the other hand, to herald these states with off-the-shelf silicon-based detectors at around 800 nm. Together with two home-deposited end-face coatings for close-to-perfect incoupling and outcoupling of the respective wavelengths, our device is a potential candidate to serve as a basic building block in more complex and miniaturized quantum network realizations in the future.

## 2. Device design, characterization method and technology

Our PDC source basically consists of two integrated building blocks. Figure 1 shows the general design of the whole device. In the periodically poled area (the first building block) the PDC process takes place and the integrated S-bend-type wavelength division demultiplexer (WDM coupler, the second building block) allows for subsequent spatial separation of signal and idler photons. Home-deposited high-quality optical end-face coatings provide our PDC source with low coupling losses of the respective colors.

### 2.1. The first building block—the parametric down-conversion process

In $\chi^{(2)}$-nonlinear lithium niobate, PDC represents a three-wave-mixing process, where one pump photon (p) decays into two daughter photons, commonly labeled signal (s) and idler (i) with the signal photon having the higher angular frequency. For this process, the conservation of photon energy

$$\hbar\omega_{\mathrm{p}} = \hbar\omega_{\mathrm{s}} + \hbar\omega_{\mathrm{i}} \qquad (1)$$

must be fulfilled.

In waveguides, the momentum conservation of the collinear traveling waves can be represented by the corresponding effective refractive indices of the individual guided modes

of pump, signal and idler beams. For the ferroelectric lithium niobate the occurring phase mismatch

$$\Delta k = k\left(\lambda_{\mathrm{p}}\right) - k\left(\lambda_{\mathrm{s}}\right) - k\left(\lambda_{\mathrm{i}}\right) \tag{2}$$

caused by dispersion, can be compensated by periodical inversion of the spontaneous material polarization, such that a first-order quasi-phasematching with

$$\Delta k - \frac{2\pi}{\Lambda_{\mathrm{G}}} = 0 \tag{3}$$

for the appropriate period $\Lambda_{\mathrm{G}}$ of the inverted domains is achieved. The technology for achieving periodic poling is explained in more detail in section 2.4.

Quasi-phasematching allows for arbitrary wavelength combinations by choosing appropriate poling periods. However, short pump wavelengths in the visible regime require small poling periods. For fixed poling periods and pump wavelengths, the wavelength combination of signal and idler is determined. In this case, wavelength tuning of the signal and idler wavelength is only possible thermally due to the temperature dependence of the effective refractive indices.

Here we focus on a type-I PDC process, in which pump photons at 532 nm wavelength decay into non-degenerate signal and idler photons of transverse magnetic (TM) polarization, accessing the highest nonlinear tensor element in lithium niobate $d_{33}$ for high conversion efficiencies. In order to determine the degree of non-degeneracy we varied the poling period of the device around 6.8 $\mu$m in several on-chip test structures.

## 2.2. Heralding and conditioned $g^{(2)}(0)$

In 1977, Kimble *et al* [29] demonstrated, for the first time, photon anti-bunching on sodium atomic emission. A well-established way to estimate the mean photon number of a PDC source is using the anti-correlation parameter $\alpha$. In 1986, Grangier *et al* [30] applied the concept of Clauser [31] in a Hanbury Brown-Twiss geometry [32] to characterize anti-correlation phenomena by the conditioned preparation of single-photon states. The value of $\alpha$ can be determined by relating the count rates of binary photon detectors [33] when making conditioned correlation measurements.

In our experiments, we pump our PDC source with pulsed light. For low pump powers one pair of photons is generated with a probability much lower than unity and higher photon number contributions are insignificant. When increasing the pump power, higher pair generation rates are possible, but at the cost of increasing higher-order components. These are detrimental to the quality of the heralded single photons, such that the appearing higher-order photon pairs should be carefully quantified.

Note that in the following we do not distinguish between the terms *trigger*, *signal photons* and *heralding photons* anymore.

The scheme of our heralded single-photon preparation is shown in figure 2 (left), where the Si-avalanche photodiode (APD) measures a detection rate $R_{\mathrm{Si}}$ with an efficiency $\eta_{\mathrm{Si}}$. The two InGaAs-APDs are conditioned on a Si-APD detection event and register the rates of the collected idler photons $R_{\mathrm{Id},1}$ and $R_{\mathrm{Id},2}$. We assume similar detection efficiencies $\eta_{\mathrm{Id1}} = \eta_{\mathrm{Id2}} = \eta_{\mathrm{Id}}$ for both InGaAs detectors and neglect the influence of dark counts. Since the idler photons are sent through a 50/50 beamsplitter in front of the detection, the rates $R_{\mathrm{Id},1}$ and $R_{\mathrm{Id},2}$ individually reflect genuine photon pair generation events, whereas threefold coincidences between all
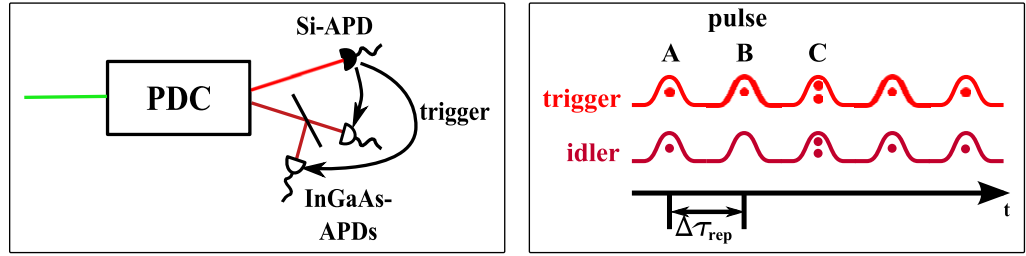
**Figure 2.** Conditioned PDC detection scheme (left); temporal PDC event behavior with a pulsed pump (right).

detectors indicate the generation of at least two photon pairs in the PDC process. These occur with the rate $R_c$. In this setting, the anti-correlation parameter $\alpha$ is given by [30, 33]

$$\alpha = \frac{R_{Si} R_c}{R_{Id,1} R_{Id,2}}. \tag{4}$$

For judging the amount of higher-order photon components in the generated PDC state, we can utilize the second-order auto-correlation or Glauber function $g^{(2)}(0)$. For our measurement scheme, it has been shown, for example in [34], that $g^{(2)}(0)$ is given by

$$g^{(2)}(0) \simeq 4 \frac{R_{Si} \cdot R_c}{(R_{Id,1} + R_{Id,2})^2} \tag{5}$$

if we assume that the probability for the generation of higher-order components is much smaller than that for the generation of single-photon pairs. Note that, in the case discussed here, the two values $\alpha$ and $g^{(2)}(0)$ are both measures for the ratio between photon pairs and unwanted higher-order components, although they are derived from different conceptual approaches.

The Klyshko efficiency [35] $\eta_K$ of the idler arm is given by

$$\eta_K = \frac{R_{Id,1} + R_{Id,2}}{R_{Si}} \tag{6}$$

and is a general measure for generation of single-photon pairs. Since our InGaAs-APDs have efficiencies below 1, we also calculate the heralding efficiency

$$\eta_H = \frac{\eta_K}{\eta_{Id}}, \tag{7}$$

which describes the performance of the single-photon preparation in our experimental setup.

Like in continuous wave experiments, the coincidences-to-accidentals ratio (CAR) provides valuable information about the performance of our PDC source, but the fact that we work with pulsed light requires a careful definition of CAR in our experiment. Figure 2 (right) schematically illustrates the typical measurement results. From this, we immediately see that the CAR is dependent on the relative time delay between signal and idler detection.

When shifting the delay of the trigger pulse $A$ and the measured correlated idler gradually to a point between two idler pulses, we expect decreasing Klyshko and heralding efficiencies. Relating the maximum Klyshko efficiency (i.e. perfect pulse overlap) to the minimum Klyshko efficiency, we obtain

$$CAR_{\Delta\tau} = \frac{\eta_K(P_p, \Delta\tau = 0)}{\eta_K(P_p, \Delta\tau = T)}, \tag{8}$$

where $|T|$ must be larger than the gating time window width but smaller than the repetition time $\tau_{rep}$ of our pump. Whenever parasitic fluorescence with long lifetimes is induced, $CAR_{\Delta\tau}$ will drop significantly due to artificial coincidences outside the region of perfect temporal pulse overlap. Note that our definition of $CAR_{\Delta\tau}$ is equivalent to the inverse output noise factor (ONF), defined in [36] and used for heralded single-photon sources working in the continuous wave (cw) regime [37].

By defining a different $CAR_{rep}$, we indirectly get information about two-photon-pair contributions if we shift the relative time delay such that pulse $A$ overlaps with the neighboring pulse $B$, given by an integer multiple of the repetition time $\tau_{rep}$. Then, detected coincidences originate from non-correlated PDC events. From the expression

$$CAR_{rep} = \frac{R_{c,double}(P_p, \Delta\tau = 0)}{R_{c,double}(P_p, \Delta\tau = m\,\tau_{rep})} \quad m \in \mathbb{N}, \tag{9}$$

we can deduce the photon pair generation probability $p$, which is closely linked to the mean photon number per pulse and hence to the brightness of our source. The value of $CAR_{rep}$ must be the same, regardless of the number of skipped pulses.

A third CAR evolves as a general measure of higher-order photon contributions if we relate the rate of all twofold coincidences $R_{c,double}$ to the rate of unwanted threefold coincidences $R_c$ at perfect temporal pulse overlap (i.e. $\Delta\tau = 0$). The purity of our source—in addition to the $g^{(2)}(0)$ value—is then characterized by

$$CAR_{HOP} = \frac{R_{c,double}(P_p, \Delta\tau = 0)}{R_c(P_p, \Delta\tau = 0)}. \tag{10}$$

The value of $CAR_{HOP}$ is expected to drop drastically with increasing pump powers according to the increasing generation of higher-order photon pairs. Note that, for the case of perfect detectors, $CAR_{rep}$ and $CAR_{HOP}$ result in exactly the same values, whereas deviations of this equality can be attributed solely to imperfect detectors.

## 2.3. The second building block—the wavelength division demultiplexer (WDM) coupler

In order to separate signal and idler photons spatially, we implemented a passive demultiplexer (WDM coupler) behind the periodically poled area.

The most accurate way to treat a waveguide directional coupler is to describe its properties in terms of local normal modes of the dual channel structure [38–40]. In our case the local normal modes comprise a symmetric (00) and an anti-symmetric (10) mode, as shown in figure 3. For sufficiently large channel gaps $d$ compared to the mode size, the propagation constants of the two modes are degenerate.

The launching of light into one input channel O is described by constructive interference of these local normal modes in the launching channel and a destructive interference in the cross channel X. Upon approaching of the two channels toward the homogeneous central section of the coupler, the degeneracy of the propagation constants of the two modes is gradually removed, as the propagation constants exponentially depend on the center-to-center distance $d(z)$. This causes an increasing amount of phase difference

$$\Delta\phi = \int_{z_1}^{z_2} (\beta_{00}(d(z)) - \beta_{10}(d(z)))\,dz \neq 0 \tag{11}$$
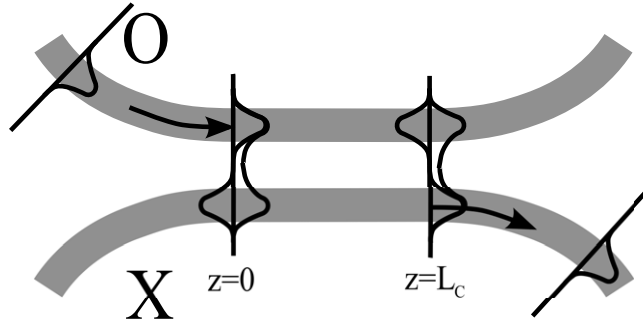
**Figure 3.** Details of the WDM coupler (left); local normal mode evolution scheme (right).

and the corresponding interference change between the two modes. As a result the power flow gradually bounces from the launching channel to the adjacent one. Complete overcoupling to the cross channel is achieved when the accumulated phase difference is $\Delta\phi = \pi$. From this we can deduce that the power flux will oscillate with a squared sinusoidal behavior dependent on the coupler stem length $L_C$.

Applying finite element method (FEM) calculations [40, 41], we anticipated the respective propagation parameters very precisely. For our non-degenerate PDC process, we designed the coupler such that first-order coupling is only provided for the fundamental waveguide mode at the idler wavelength whereas the signal power almost fully remains in the original channel due to the stronger confinement at the shorter signal wavelength. Bending losses are circumvented by the implementation of S-bend input and output ports with sufficiently large radii of curvature [42]. On our chip we only varied the coupler stem length from $2750\,\mu\text{m} \leqslant L_C \leqslant 4250\,\mu\text{m}$ at a fixed center-to-center gap of $13\,\mu\text{m}$ within different test structures to determine the optimum coupling behavior of the idler wavelength, which is shown schematically in figure 3. Fixing the output port gap to a value of $165\,\mu\text{m}$ provides us with the opportunity for a direct fiber connection via silicon V-groves.

As a measure of the demultiplexing dependence on the coupler's stem length $L_C$, we define the power suppression in the unwanted output ports using a logarithmic scaling, where

$$S_s = 10 \times \log\left(\frac{P_X(L_C, \lambda_s)}{P_O(L_C, \lambda_s)}\right) \tag{12}$$

denotes the signal suppression in the cross port (X) and

$$S_i = 10 \times \log\left(\frac{P_O(L_C, \lambda_i)}{P_X(L_C, \lambda_i)}\right) \tag{13}$$

denotes the idler suppression in the original port (O).

We carefully analyzed the coupling properties using classical light. It turned out that the power suppression in the unwanted WDM output ports does depend on the stem length $L_C$ as expected (see figure 4). In the optimum case at $L_C = 4000\,\mu\text{m}$, we get close-to-perfect coupling behavior for both, signal and idler. While the signal remains with a ratio of $\eta_{\text{WDM,s}} = 96.5\%$ in the original channel, the idler couples by $\eta_{\text{WDM,i}} = 99.1\%$ to the cross channel, corresponding to suppressions of $S_{\text{s,opt}} = -15\,\text{dB}$ and $S_{\text{i,opt}} = -20.6\,\text{dB}$, respectively.
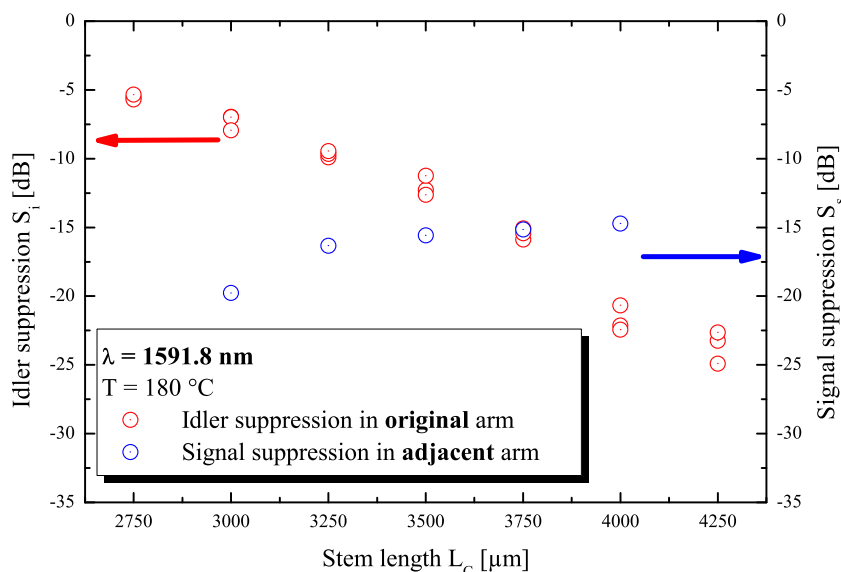
**Figure 4.** WDM coupler characteristics for signal (red) and idler (blue).

## 2.4. Waveguide, WDM and poling technology

The realization of low-loss waveguides and WDM coupler structures for efficient type-I PDC has been achieved using Z-cut lithium niobate propagation along the $x$-direction.

In our specific case, titanium of 80 nm homogeneous thickness was deposited by electron beam evaporation onto the Z-surface of the substrate. The waveguide structure was defined by photolithograpic delineation of the titanium layer using deep UV contact printing. The residual Ti stripes were indiffused at 1060 °C for 8.5 h in an oxygen-rich atmosphere, allowing for the idler wave to be guided in its fundamental spatial mode, whereas pump and signal photons can be guided in multiple modes.

For periodic poling the standard electric field-assisted poling method [43] was applied, using a waveguide selective segmented resist patterning for electrical insulation and lithium chloride solution as the contact electrolyte. By applying short voltage pulses of 11.5 kV and monitoring the displacement current due to the periodic polarization reversal, the accumulated charge was controlled to provide the proper duty cycle of the 30 mm long domain grating. A typical poling structure is visualized in figure 5 (left).

In order to achieve the best possible coupling of light into and out of the waveguides, the end-facettes were polished perpendicularly to the propagation direction. We designed and deposited different end-face coatings for optimized incoupling of the pump as well as for the best possible outcoupling of signal and idler wavelengths including the reflection of the pump. The transmission characteristics for both coatings are shown in figure 5 (right). Note that the coating at the waveguide output reaches more than 99% of reflection for the pump, while the idler wavelength is transmitted with more than 96.5%.

An important linear optical feature of the waveguides is their low intrinsic loss of 0.07 dB cm$^{-1}$ on average, which we measured for straight control channels next to the coupler structures. For this measurement, we applied the well-established low-finesse Fabry–Pérot interferometric method [28].
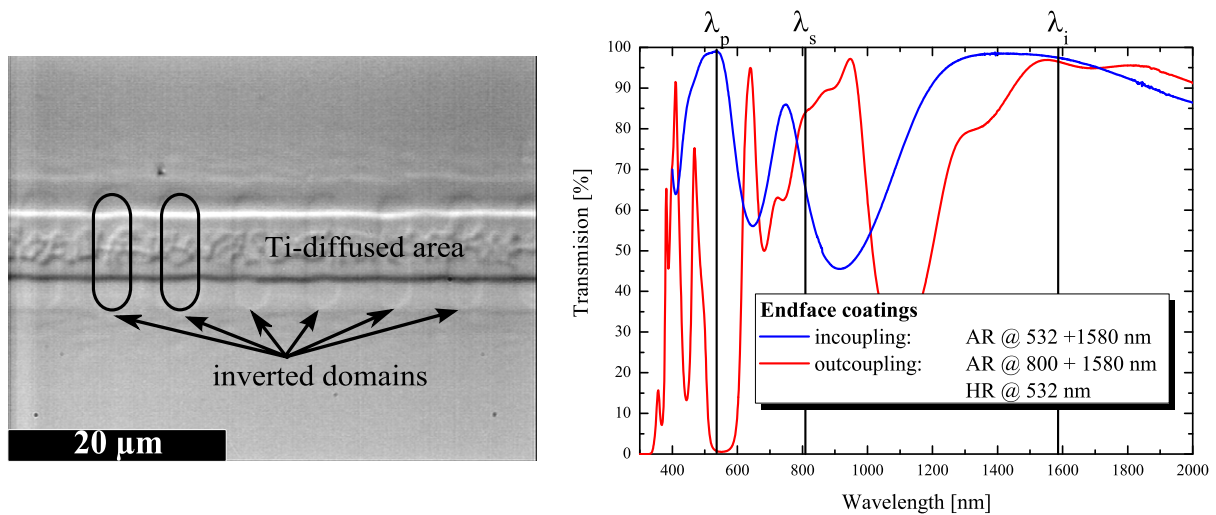
**Figure 5.** Domain structure of the periodically poled waveguide area (left); characteristics of the end-face coatings (right).

An issue for later nonlinear measurements arises from the fact that the mode size of the idler wave and its symmetry are both important for the coupling to single-mode fibers (SMFs), since any asymmetry decreases the overlap. Therefore, we measured the waveguide mode sizes at the idler wavelength and calculated a theoretical mode overlap integral to standard SMFs in TM polarization of 90.1%, which is the benchmark for the Klyshko efficiency under the assumption of perfect transmission in the idler beam path and perfect detectors.
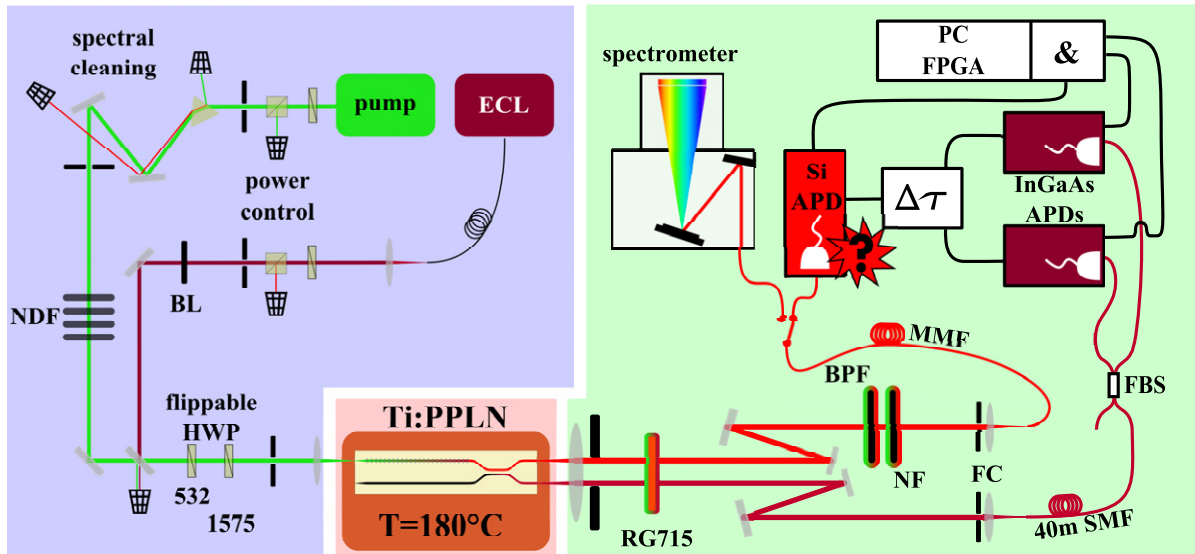
## 3. Experimental setup

Figure 6 illustrates our experimental setup, which can be divided into three major divisions: incoupling, sample adjustment and analysis part.

We used a frequency-doubled pump source (Katana-05, Onefive GmbH Zürich), which converts amplified diode laser light at 1064 nm to the green in a second harmonic generation process. The laser is running at 10 MHz repetition rate with Fourier-limited pulses of 43 ps duration and a Gaussian shape. Its spectral width is specified with 0.19 nm while it offers a low pulse-to-pulse timing jitter of less than 10 ps. In order to spectrally filter out any residual 1064 nm pump light, we added a prism-based cleaning stage in front of a variable attenuator and neutral density filters, which allow for additional power control. The required TM polarization for the type-I PDC process is set using a $\lambda/2$-plate right in front of an anti-reflection (AR)-coated incoupling lens.

The PDC source is stabilized at $T_{OP} = (185 \pm 0.2)\,°C$ on a home-assembled five-axis stage with high precision. The analysis part of the setup is kept in a free-space configuration as far as possible.

Right behind the AR-coated outcoupling lens we placed a home-deposited RG715 filter, which transmits signal and idler with 97% and has an overall pump suppression larger than six orders of magnitude.

Two D-shaped mirrors further split up the on-chip spatially separated beams into a signal and an idler arm. The signal arm consists of a multi-mode fiber coupling stage, which

**Figure 6.** Experimental setup for spectral characterization and conditioned measurements. NDF: neutral density filters; BL: beam blocker; ECL: external cavity laser for idler coupling adjustment; HWP: half-wave plate; RG715: customized absorptive filter; NF: needle filter; BPF: band-pass filter; FC: fiber coupling stages; SMF: single-mode fiber; MMF: multi-mode fiber; FBS: fiber beamsplitter 50/50; $\Delta\tau$: delay generator; APD: avalanche photodiode; FPGA: field programmable gate array.

is connected to a spectrometer system (Andor iKon-M 934P-DD/Shamrock SR-303iA) for spectral PDC characterization. It can also be connected to the free-running silicon avalanche photo diode (Si-APD, Perkin Elmer SPCM-AQRH-13) for the heralding experiments and for conditioned $g^{(2)}(0)$ measurements at room temperature. The Si-APD is specified to have a detection efficiency of $\eta_{Si}(\lambda_s) = 55\%$ at around 800 nm and was measured to have an average dark count rate of $R_{T,dark} = (238 \pm 16)\,s^{-1}$. To extract the PDC signal photons from any noisy background in the heralding experiments, we can flip an additional bandpass filter (FWHM = 12 nm, $T_{peak} \geqslant 99.5\%$) as well as a needle filter (FWHM = 0.5 nm, $T_{peak} = 78\%$) into the signal beam path.

The idler arm also includes a high-precision fiber coupling stage for injecting the idler photons to the InGaAs-APDs (ID Quantique ID201) via 40 m of AR-coated SMF, the length of which ensures the optical compensation of electrical delays. For $g^{(2)}(0)$ measurements, a fiber beam splitter enables us to address a second InGaAs-APD. At the idler wavelength both APDs have the specified detection efficiencies of $\eta_{Id}(\lambda_i) = 0.23$. Their aquisition time gate for idler click events was set to 2.5 ns with zero additional deadtime.

Electronic compensation of the occurring temporal gap in the arrival of signal and idler at the respective detector is realized using a Stanford Research DG645 delay generator. Data acquisition and the evaluation of single and coincidence events are carried out using an FPGA interface card operating at 40 MHz.

A classical characterization of the overall idler transmission loss from the device's end-face to the InGaAs-APDs input resulted in a transmission factor of $T_i = 0.663$. This includes
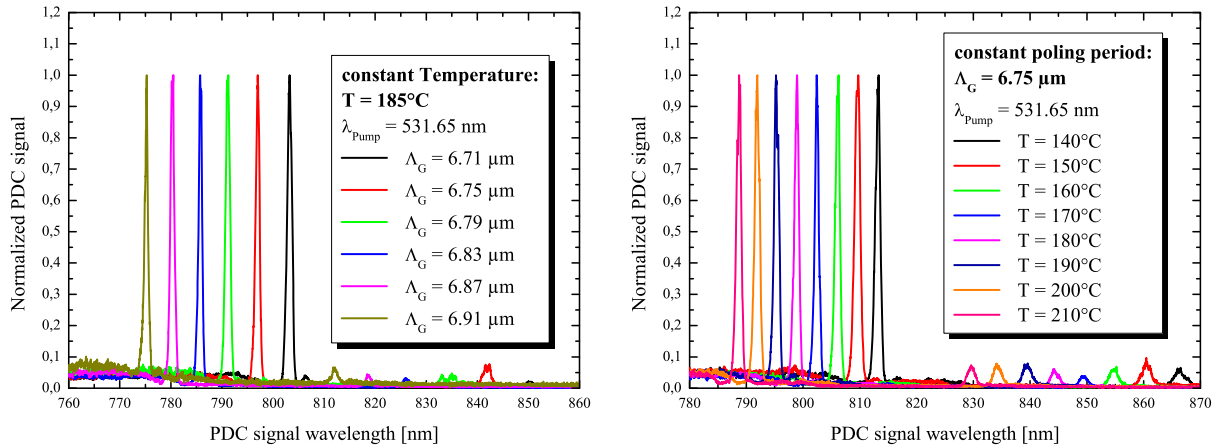
**Figure 7.** Tunability of the PDC signal wavelength with the crystal's poling period (left) and the device's temperature (right).

the device's end-face throughput as well as filters, lenses, fiber coupling and the optical loss in the fiber beamsplitter.

In contrast to the benchmarking Klyshko efficiency described in section 2.4, the maximum Klyshko efficiency of our experimental setup is limited by the overall transmission in the idler arm, by the respective detector efficiency and by the coupling efficiency of the on-chip integrated WDM coupler to

$$\eta_{\text{K,System}} = T_i \, \eta_{\text{Id}} \, (\lambda) \, \eta_{\text{WDM,i}} = 0.151,$$

resulting in a maximum achievable heralding efficiency of $\eta_{\text{H,max}} = 65.6\%$. This upper experimental boundary only holds for very low pump power levels, where higher-order photon pair contributions can be neglected.

## 4. Results and discussion

### 4.1. Spectral characteristics

The spectral dependences of the generated PDC signal on temperature and poling period have been determined and are plotted as normalized curves in figure 7. These results prove a convenient wavelength tunability to be either coarse (with poling period) or fine (with temperature). Note that there are practically no significant sidepeaks or higher-order mode excitations, indicating an excellent waveguide homogeneity and the best possible incoupling of the pump to its fundamental waveguide mode. In any case the signal FWHM is around 0.7 nm, which is mainly contributed by the on-chip nonlinear interaction length of 30 mm, while the influence of the spectral width or limiting temporal properties of the pump is neglectable. We can clearly identify a broad structure in the lower wavelength region next to the PDC signal peaks in figure 7. We suspect this to be nonlinear Cerenkov radiation associated with the quasi-phasematching process [44]. These background effects have been suppressed for the following experiments with the help of a needle filter as mentioned in section 3.
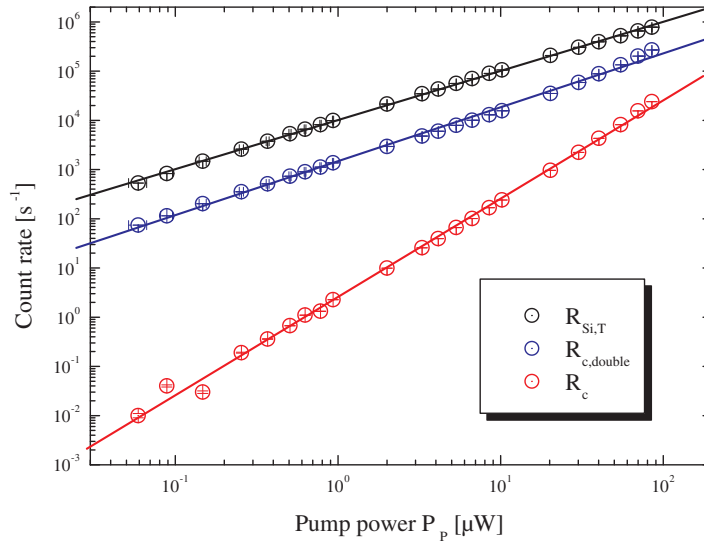
**Figure 8.** Pump-dependent count rates of the trigger (black), the sum of the twofold coincidences (blue) and the triple coincidences (red) in conditioned measurements. The solid lines serve as a guide to the eye.

### 4.2. State preparation rates

Our power-dependent $g^{(2)}(0)$-measurements yielded the trigger rates $R_{Si}$, the overall twofold coincidence rates $R_{c,double} = R_{Id,1} + R_{Id,2}$ and the triple coincidence rates $R_c$ within 1 s of measurement time. Repeating this hundredfold provides us with small error bars. The threefold coincidence rate contributes the highest uncertainties. Figure 8 shows the respective rates in double-logarithmic scaling. The trigger rate has an almost linear dependence on the increasing pump power, while the coincidence rates both increase superlinearly in the pump power range above $10\,\mu W$. Note that the linearity of the trigger rate disappears above $10^5$ counts s$^{-1}$ due to deadtime effects.

### 4.3. Heralded single-photon preparation

From the count rates we calculated the Klyshko and heralding efficiencies according to (6) and (7), which are plotted in figure 9 (left). The $g^{(2)}(0)$ values and the anti-correlation parameter $\alpha$ were calculated using (5) and (4), respectively.

We identified an almost constant heralding efficiency as high as 60% at pump powers less than $10\,\mu W$, where seemingly only first-order photon pairs contribute to the measurement (compare plots in figure 8) and the trigger rate is up to $R_{Si} = 105\,kHz$. To the best of our knowledge, this is the first time that in a Ti : PPLN-based type-I PDC source such high heralding efficiencies have been reported, while other sources using comparable detection schemes (see e.g. [45–47]) rely on bulk nonlinear materials or photonic crystal fibers and do not offer more than one integrated functionality. The coupling limitations of our laboratory system can probably be overcome when a completely fiber-based setup is used in the future. This should further improve the heralding efficiencies to around 80%.

As shown in figure 9 (right), the auto-correlation function at very low power levels ($P_p \leqslant 1\,\mu W$) reaches a minimum value of $g^{(2)}(0) = 0.0038$, which is one of the best results for
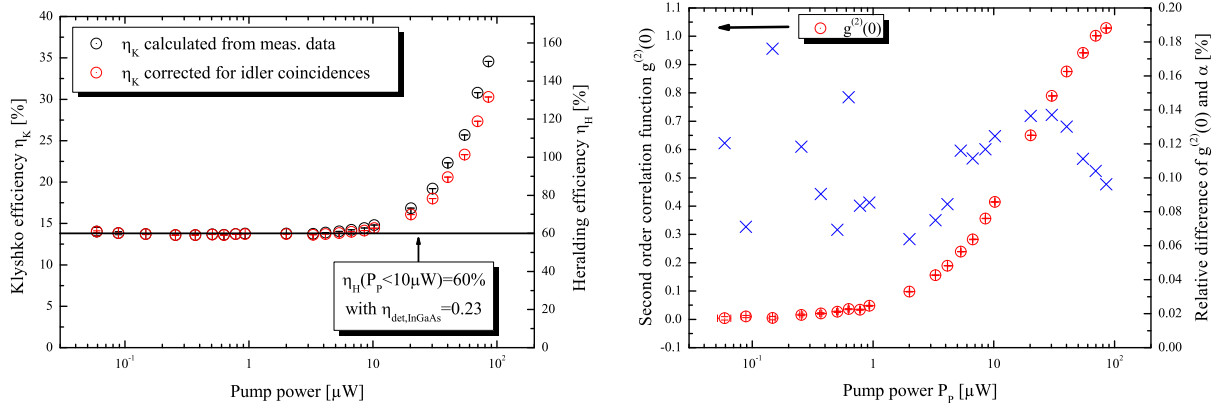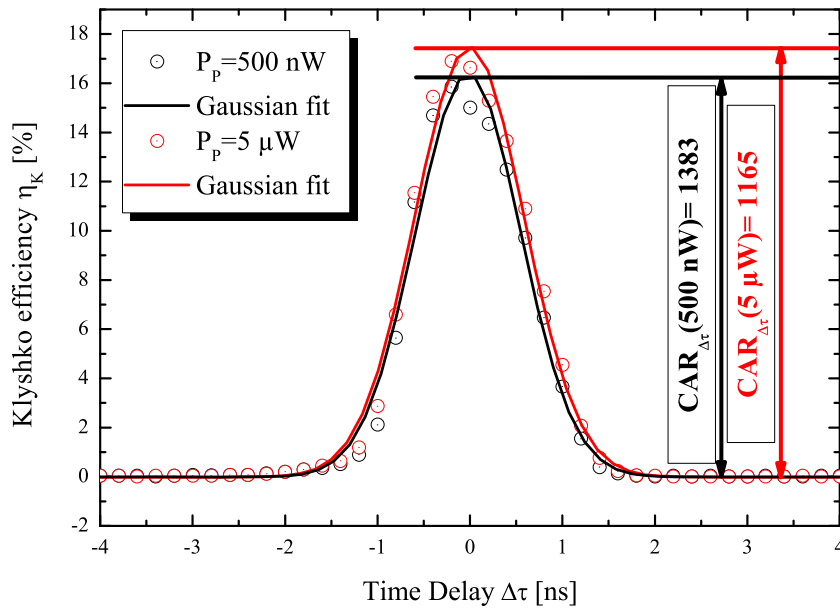
**Figure 9.** Pump-dependent Klyshko efficiency and heralding efficiency (left); auto-correlation function $g^{(2)}(0)$ and its relative difference to the anti-correlation parameter $\alpha$ (right).

heralded single-photon sources in general, while it marks the lowest obtained value in titanum-indiffused PPLN waveguide PDC sources to date. It could be driven even lower at the cost of the heralding rate. But for applications such as quantum key distribution (QKD) with this kind of PDC sources, low trigger rates are always related to low key transmission rates, and a trade-off between high rates and purity of the single photons is unavoidable.

From our results, we can conclude that the approximation made in (5) and in [33, 34] is only valid and suitable for low pump powers. At the upper end of our power scale, we see that $g^{(2)}(0)$ approaches the value of 1, which would correspond to an infinite average photon number. Note, however, that at these high pump power levels our assumption that the probability of generating higher-order photon pairs is much smaller than the probability of generating single-photon pairs is no longer valid. The triggering rate $R_{Si}$ and the triple coincidence rate $R_c$ both tend to be overestimated due to higher-order photon contributions. The Si-APD fires only once, when there is more than one trigger photon arriving and internal deadtime effects of the InGaAs-APDs limit the repetition rate of the detection of double coincidences. We can derive from the graph in figure 8 in conjunction with figure 9 (right) that trigger rates higher than 310 kHz should be avoided for this kind of detectors in combination with our kind of measurement. It also shows that the relative differences between the calculated values of $g^{(2)}(0)$ and the anti-correlation parameter $\alpha$ are very small, which is a proof of the equivalence of (4) and (5) for our measurements.

### 4.4. Measurement of coincidences-to-accidentals ratios

For the analysis of detrimental background photons, we determined the source's heralding efficiency around the optimum time delay between trigger and heralded photons at two different power levels, measuring the count rates in step widths of 0.2 ns for 5 s, each. The characteristics in figure 10 show almost a Gaussian shape. This is mainly caused by the intrinsic gate width of the InGaAs-APDs of $\tau_{gate} = (1.16 \pm 0.32)$ ns, where the error includes the timing jitter of the InGaAs-APD, the Si-APD and of the delay generator. The graph visualizes the slight increase of the Klyshko efficiency with increased pump power due to higher-order photon pair contributions. In figure 11 we see that the Klyshko efficiency is almost not affected by

**Figure 10.** Dependence of the Klyshko efficiency on the temporal overlap between signal and idler detection.
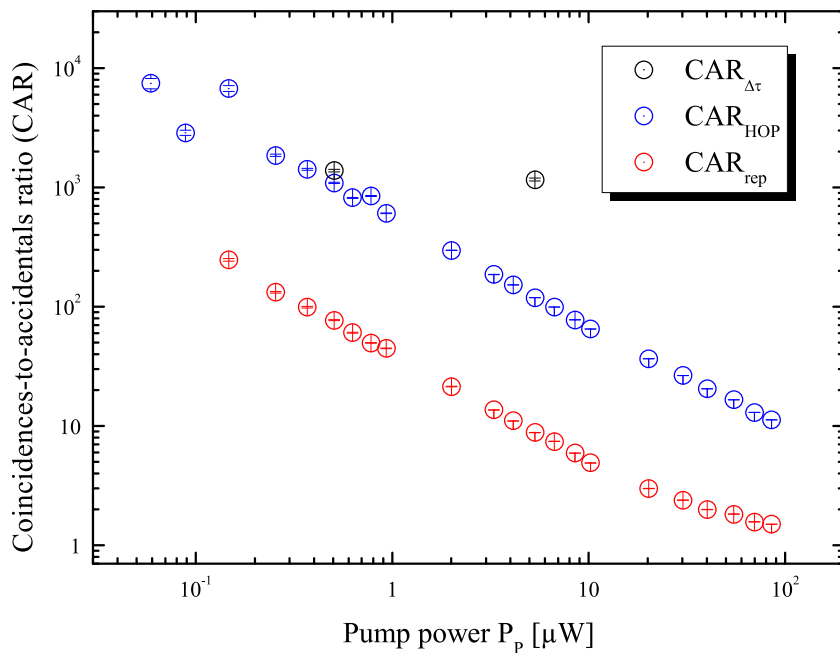


**Figure 11.** Pump dependence of the three calculated CARs.

pump-induced fluorescence of any optical component. In particular, at 500 nW and 5 μW, the $CAR_{\Delta\tau}$ have been calculated to be 1383 and 1165, respectively, and thus do not decrease significantly. Please note that in figure 10 this feature cannot to be seen intuitively due to the scaling of the accidentals. Inverting the $CAR_{\Delta\tau}$ values provides us with ONFs of 0.072 and 0.086%, respectively, which are both a factor of 3 smaller than the best ONFs in comparable cw
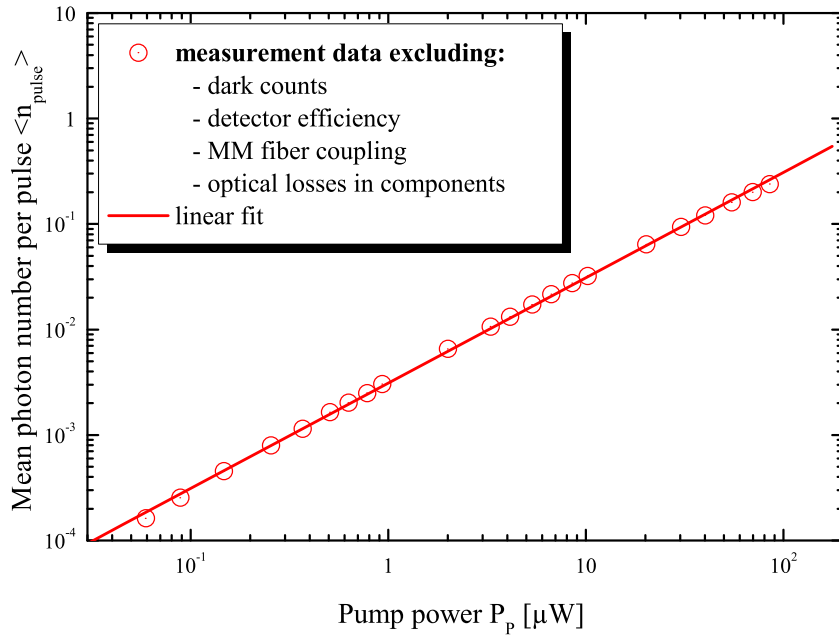
**Figure 12.** Linear dependence of a pulse's average photon number on increasing pump power.

experiments [37]. Together with the fact that we are still in the single-photon regime ($0.027 \leqslant g^{(2)}(0) \leqslant 0.24$) and with the high heralding rates $5.3\,\mathrm{kHz} \leqslant R_{\mathrm{Si}} \leqslant 56\,\mathrm{kHz}$, this impressively points out the benefits of heralding single-photon experiments in the pulsed regime.

Figure 11 shows that the $\mathrm{CAR}_{\mathrm{rep}}$ for two adjacent pulses asymptotically tends to the value of 1 at the highest suitable pump power, while the $\mathrm{CAR}_{\mathrm{HOP}}$ dropped from 7440 to around 10. This emphasizes the impact of higher-order photon contributions and the usefulness of a trade-off between high heralding rates and a low $g^{(2)}(0)$.

One of the most important and remarkable figures of merit of our source is its brightness. We determined the pump-dependent mean number of generated photons per pulse by dividing the heralding rate $R_{\mathrm{Si}}$ by the transmissivities of all optical components in the signal arm and by the repetition rate $R_{\mathrm{rep}} = 10\,\mathrm{MHz}$, which is shown in figure 12. We identified a maximum mean photon number per pulse of $\langle n_{\mathrm{pulse,max}} \rangle = 0.24$ at the highest applied pump power of $85.14\,\mu\mathrm{W}$. A linear extrapolation yields an average photon number per pulse of $\langle n_{\mathrm{pulse,th}} \rangle \approx 34$ at $P_{\mathrm{P}} = 10\,\mathrm{mW}$ of cw-equivalent pump power, which is easily available with our pump laser.

## 5. Conclusion and outlook

We demonstrated the on-chip integration of an efficient waveguide-based type-I PDC source in combination with a passive WDM coupler for spatial separation of signal and idler photons. It shows close-to-perfect demultiplexing behavior at wavelengths of 803 and 1575 nm as well as very low scattering loss. We achieved high heralding efficiencies of 60% in conjunction with a second-order auto-correlation function as low as 0.0038. At pump power levels below $10\,\mu\mathrm{W}$ only a minor influence of higher-order photon pairs to the detection can be deduced from the results. We determined a coincidence-to-accidentals ratio of $\mathrm{CAR}_{\mathrm{HOP}} > 7400$ at low power

levels and output noise factors ONF < 0.1% in the regime of low auto-correlation function values for our pulsed experiments. This indicates almost pure single-photon pair generation together with high (although unoptimized) heralding rates as well as practically no influence of background noise.

The high brightness of the source was derived from the extrapolation of the mean photon number per pulse of $\langle n_{\text{pulse,th}} \rangle \approx 34$ at $P_{\text{P}} = 10\,\text{mW}$ cw-equivalent pump power.

At higher power levels $P_{\text{P}} \geqslant 30\,\mu\text{W}$ our commercially available Si- and InGaAs-detectors tend to saturate, which distorts the calculation of correct $g^{(2)}(0)$ values, while the detection part of our analysis seems to be the limiting factor in terms of temporal resolution and dark counts. This limitation could be lifted in the future by novel detectors exhibiting drastically improved temporal properties (e.g. in [48, 49]) in conjunction with a careful characterization of photon statistics using photon number resolving detection schemes (see [50–52]). Then pump lasers with higher clock rates could yield higher heralding rates, which would be required for the commercialization, e.g., of quantum cryptography applications.

Besides, more difficulties can arise in the used heralding scheme with regard to the transmission of timing information within a wide-area quantum network (compare [53]). Note, however, that—in contrast to cw realizations—in our pulsed scheme an intrinsic clock can be transferred from sender to receiver for the security of commercial QKD systems (compare e.g. [54]).

Due to the strong dependence of the heralding efficiency on the coupling of the heralded photons to optical fibers, we will proceed in our work with the implementation of an all-fiber-connected device. This could increase the heralding efficiency to around 80%.

The general design of our device together with its figures of merit constitute an important step for the implementation of integrated sources with multiple functionalities in future quantum networks with miniaturized nodes. Additional functionalities such as electro-optic phase shifters or polarization controllers in combination with passively working add-ons such as polarization splitters and sophisticated end-face coatings could open up new routes to establish quantum networks with novel node architectures.

## Acknowledgments

## References

[1] Tanzilli S, Martin A, Kaiser F, De Micheli M P, Alibart O and Ostrowsky D B 2012 On the genesis and evolution of integrated quantum optics *Laser Photon. Rev.* **6** 115–43

[2] Martin A, Alibart O, De Micheli M P, Ostrowsky D B and Tanzilli S 2012 A quantum relay chip based on telecommunication integrated optics technology *New J. Phys.* **14** 025002

[3] Christ A and Silberhorn C 2012 Limits on the deterministic creation of pure single-photon states using parametric down-conversion *Phys. Rev.* A **85** 023829

[4] Sangouard N, Sanguinetti B, Curtz N, Gisin N, Thew R and Zbinden H 2011 Faithful entanglement swapping based on sum-frequency generation *Phys. Rev. Lett.* **106** 120403

[5] Bonneau D *et al* 2012 Quantum interference and manipulation of entanglement in silicon wire waveguide quantum circuits *New J. Phys.* **14** 045003

[6] Pomarico E, Sanguinetti B, Guerreiro T, Thew R and Zbinden H 2012 Mhz rate and efficient synchronous heralding of single photons at telecom wavelengths *Opt. Express* **20** 23846–55

[7] Politi A, Cryan M J, Rarity J G, Yu S and O'Brien J L 2008 Silica-on-silicon waveguide quantum circuits *Science* **320** 646

[8] Marshall G D, Politi A, Matthews J C F, Dekker P, Ams M, Withford M J and O'Brien J L 2009 Laser written waveguide photonic quantum circuits *Opt. Express* **17** 12546–54

[9] Peruzzo A, Laing A, Politi A, Rudolph T and O'Brien J L 2011 Multimode quantum interference of photons in multiport integrated devices *Nature Commun.* **2** 224

[10] Matthews J C F, Politi A, Stefanov A and O'Brien J L 2009 Manipulation of multiphoton entanglement in waveguide quantum circuits *Nature Photon.* **3** 346–50

[11] Shadbolt P, Vértesi T, Liang Y-C, Branciard C, Brunner N and O'Brien J L 2012 Guaranteed violation of a bell inequality without aligned reference frames or calibrated devices *Sci. Rep.* **2** 470

[12] Li H W, Przeslak S, Niskanen A O, Matthews J C F, Politi A, Shadbolt P, Laing A, Lobino M, Thompson M G and O'Brien J L 2011 Reconfigurable controlled two-qubit operation on a quantum photonic chip *New J. Phys.* **13** 115009

[13] Smith B J, Kundys D, Thomas-Peter N, Smith P G R and Walmsley I A 2009 Phase-controlled integrated photonic quantum circuits *Opt. Express* **17** 13516–25

[14] Metcalf B J *et al* 2012 Multi-photon quantum interference in a multi-port integrated photonic device arXiv:1208:4575

[15] Spring J B *et al* 2013 Boson sampling on a photonic chip *Science* **339** 798–801

[16] Tanzilli S, De Riedmatten H, Tittel H, Zbinden H, Baldi P, De Micheli M, Ostrowsky D B and Gisin N 2001 Highly efficient photon-pair source using periodically poled lithium niobate waveguide *Electron. Lett.* **37** 26–8

[17] Banaszek K, U'Ren A B and Walmsley I A 2001 Generation of correlated photons in controlled spatial modes by downconversion in nonlinear waveguides *Opt. Lett.* **26** 1367–9

[18] Booth M C, Atatüre M, Giuseppe G Di, Saleh B E A, Sergienko A V and Teich M C 2002 Counterpropagating entangled photons from a waveguide with periodic nonlinearity *Phys. Rev.* A **66** 023815

[19] Chen J, Pearlman A J, Ling A, Fan J and Migdall A L 2009 A versatile waveguide source of photon pairs for chip-scale quantum information processing *Opt. Express* **17** 6727–40

[20] Bonneau D, Lobino M, Jiang P, Natarajan C M, Tanner M G, Hadfield R H, Dorenbos S N, Zwiller V, Thompson M G and O'Brien J L 2012 Fast path and polarization manipulation of telecom wavelength single photons in lithium niobate waveguide devices *Phys. Rev. Lett.* **108** 053601

[21] Kaiser F, Issautier A, Ngah L A, Danila O, Herrmann H, Sohler W, Martin A and Tanzilli S 2012 High-quality polarization entanglement state preparation and manipulation in standard telecommunication channels *New J. Phys.* **14** 085015

[22] Karpinski M, Radzewicz C and Banaszek K 2012 Dispersion-based control of modal characteristics for parametric down-conversion in a multimode waveguide *Opt. Lett.* **37** 878–80

[23] Solntsev A S, Sukhorukov A A, Neshev D N and Kivshar Y S 2012 Spontaneous parametric down-conversion and quantum walks in arrays of quadratic nonlinear waveguides *Phys. Rev. Lett.* **108** 023601

[24] Pomarico E, Sanguinetti B, Gisin N, Thew R, Zbinden H, Schreiber G, Thomas A and Sohler W 2009 Waveguide-based OPO source of entangled photon pairs *New J. Phys.* **11** 113042

[25] Alibart O, Ostrowsky D B, Baldi P and Tanzilli S 2005 High-performance guided-wave asynchronous heralded single-photon source *Opt. Lett.* **30** 1539–41

[26] Martin A, Issautier A, Herrmann H, Sohler W, Ostrowsky D B, Alibart O and Tanzilli S 2010 A polarization entangled photon-pair source based on a type-II PPLN waveguide emitting at a telecom wavelength *New J. Phys.* **12** 103005

[27] Fiorentino M, Spillane S M, Beausoleil R G, Roberts T D, Battle P and Munro M W 2007 Spontaneous parametric down-conversion in periodically poled KTP waveguides and bulk crystals *Opt. Express* **15** 7479–88

[28] Regener R and Sohler W 1985 Loss in low-finesse Ti:LiNbO$_3$ optical waveguide resonators *Appl. Phys.* B **36** 143–7

[29] Kimble H J, Dagenais M and Mandel L 1977 Photon antibunching in resonance fluorescence *Phys. Rev. Lett.* **39** 691–5

[30] Grangier P, Roger G and Aspect A 1986 Experimental evidence for a photon anticorrelation effect on a beam splitter: a new light on single-photon interferences *Europhys. Lett.* **1** 173

[31] Clauser J F 1974 Experimental distinction between the quantum and classical field-theoretic predictions for the photoelectric effect *Phys. Rev.* D **9** 853–60

[32] Hanbury Brown R Q and Twiss R 1956 Correlation between photons in two coherent beams of light *Nature* **177** 27–9

[33] U'Ren A B, Silberhorn C, Ball J L, Banaszek K and Walmsley I A 2005 Characterization of the nonclassical nature of conditionally prepared single photons *Phys. Rev.* A **72** 021802

[34] Fasel S, Alibart O, Tanzilli S, Baldi P, Beveratos A, Gisin A and Zbinden H 2004 High-quality asynchronous heralded single-photon source at telecom wavelength *New J. Phys.* **6** 163

[35] Klyshko D N 1980 Use of two-photon light for absolute calibration of photoelectric detectors *Sov. J. Quantum Electron.* **10** 1112

[36] Brida G, Degiovanni I P, Genovese M, Migdall A, Piacentini F, Polyakov S V and Berchera I R 2011 Experimental realization of a low-noise heralded single-photon source *Opt. Express* **19** 1484–92

[37] Brida G *et al* 2012 An extremely low-noise heralded single-photon source: a breakthrough for quantum technologies *Appl. Phys. Lett.* **101** 221112

[38] Marcatili E A J 1969 Dielectric rectangular waveguide and directional coupler for integrated optics *Bell Syst. Tech. J.* **48** 2071–102

[39] Burns W K, Milton A F, Lee A B and West E J 1976 Optical modal evolution 3 db coupler *Appl. Opt.* **15** 1053–65

[40] Bersiner L, Hempelmann U and Strake E 1991 Numerical analysis of passive integrated-optical polarization splitters: comparison of finite-element method and beam-propagation method results *J. Opt. Soc. Am.* B **8** 422–33

[41] Strake E, Bava G P and Montrosset I 1988 Guided modes of Ti:LiNbO$_3$ channel waveguides: a novel quasi-analytical technique in comparison with the scalar finite-element method *Light. Technol. J.* **6** 1126–35

[42] Tsao S-L and Lu C-Y 2002 Bpm simulation and comparison of $1 \times 2$ directional waveguide coupling and y-junction coupling silicon-on-insulator optical couplers *Fiber Integr. Opt.* **21** 417–33

[43] Yamada M, Nada N, Saitoh M and Watanabe K 1993 First-order quasi-phase matched LiNbO$_3$ waveguide periodically poled by applying an external field for efficient blue second-harmonic generation *Appl. Phys. Lett.* **62** 435–6

[44] Zhang Y, Gao Z D, Qi Z, Zhu S N and Ming N B 2008 Nonlinear cerenkov radiation in nonlinear photonic crystal waveguides *Phys. Rev. Lett.* **100** 163904

[45] Mosley P J, Lundeen J S, Smith B J, Wasylczyk P, U'Ren A B, Silberhorn C and Walmsley I A 2008 Heralded generation of ultrafast single photons in pure quantum states *Phys. Rev. Lett.* **100** 133601

[46] Söller C, Cohen O, Smith B J, Walmsley I A and Silberhorn C 2011 High-performance single-photon generation with commercial-grade optical fiber *Phys. Rev.* A **83** 031806

[47] Steinlechner F *et al* 2012 A high-brightness source of polarization-entangled photons optimized for applications in free space *Opt. Express* **20** 9640–9

[48] Verma V B, Marsili F, Harrington S, Lita A E, Mirin R P and Nam S W 2012 A three-dimensional, polarization-insensitive superconducting nanowire avalanche photodetector *Appl. Phys. Lett.* **101** 251114

[49] Marsili F *et al* 2012 Detecting single infrared photons with 93% system efficiency arXiv:1209.5774

[50] Achilles D, Silberhorn C, Śliwa C, Banaszek K and Walmsley I A 2003 Fiber-assisted detection with photon number resolution *Opt. Lett.* **28** 2387–9

[51] Fitch M J, Jacobs B C, Pittman T B and Franson J D 2003 Photon-number resolution using time-multiplexed single-photon detectors *Phys. Rev.* A **68** 043814

[52]  Mauerer W and Silberhorn C 2007 Quantum key distribution with passive decoy state selection *Phys. Rev.* A **75** 050305

[53]  Giustina M *et al* 2012 Bell violation with entangled photons, free of the fair-sampling assumption arXiv:1212.0533

[54]  Lydersen L, Wiechers C, Wittmann C, Elser D, Skaar J and Makarov V 2010 Hacking commercial quantum cryptography systems by tailored bright illumination *Nature Photon.* **4** 686–9